Rendiconti Lincei. Scienze Fisiche e Naturali
https://doi.org/10.1007/s12210-025-01397-3

NON-DESTRUCTIVE TECHNIQUES FOR CULTURAL HERITAGE

Portable X-ray tomography prototype for cultural heritage: design and applications

A. Mazzinghi[1,2] · F. Cantini[1,2,3] · M. Massi[2] · L. Castelli[2] · M. Bettuzzi[4,5] · M. P. Morigi[4] · M. Galeotti[6] · A. Cagnini[6] · S. Porcinai[6] · M. Manetti[2] · F. Taccetti[2] · L. Giuntini[1,2]

Received: 9 October 2025 / Accepted: 4 December 2025

Abstract

X-ray radiography and tomography are widely employed techniques in the Cultural Heritage (CH) field, as testified by the large number of analyses performed for these applications in this field. Specifically, tomography provides fully non-invasive morphological and microstructural information on the internal structure of the sample and can reveal, when possible, hidden details such as ancient repairs or concealed conservation interventions. All these aspects make this technique essential both for gaining insights into production techniques and for assessing the conservation state. One of the main requirements for instrumentation employed in Heritage Science is the versatility of the equipment, as artefacts can vary considerably in size, may have complex and irregular shapes, and exhibit diverse compositions, materials, and manufacturing methods. It is therefore evident that the instrumentation must be readily adaptable to each specific application. This requirement also implies the necessity for portable and open-source equipment. The latter characteristic is of particular importance, as open-source instruments allow for extensive customisation in response to the diverse requirements of different operators. In the framework of the National recovery and Resilience Plan (PNRR) CHANGES (Cultural Heritage Innovation for Next-Gen Sustainable Society) project, a fruitful collaboration was established with the Department of Physics and Astronomy of the University of Bologna, as regards mainly the detection system, and the Opificio delle Pietre Dure (OPD), acting in the quality of end-user. Taking all the above-mentioned aspects into consideration, at the Department of Physics and Astronomy of the University of Florence and with the crucial support of the CHANGES project, we developed a portable and open-source X-ray tomography system specifically designed for Cultural Heritage applications. In this paper, we present this prototype which offers a highly customisable design that can be tailored to a wide range of operational needs.

A. Mazzinghi and F. Cantini are contributed equally to this work.

The topical collection "Non-Destructive Techniques for Cultural Heritage" is a follow-up of several conferences which hosted renowned scientist from all the world, many contributing previous papers. The aim continues to be drawing attention to a problem of great cultural interest and socioeconomic significance and building a wide net of collaborations.

✉ A. Mazzinghi
anna.mazzinghi@unifi.it

[1] Dipartimento di Fisica e Astronomia, Università degli Studi di Firenze, Sesto Fiorentino, FI, Italy

[2] Istituto Nazionale di Fisica Nucleare, Sezione di Firenze, Sesto Fiorentino, FI, Italy

[3] Istituto di Fisica Applicata Nello Carrara - Consiglio Nazionale delle Ricerche, Sesto Fiorentino, FI, Italy

[4] Dipartimento di Fisica, Università degli Studi di Bologna, Bologna, Italy

[5] Istituto Nazionale di Fisica Nucleare, Sezione di Bologna, Bologna, Italy

[6] Opificio delle pietre Dure di Firenze - Ministero della Cultura, Firenze, Italy

Published online: 24 December 2025

Graphic abstract

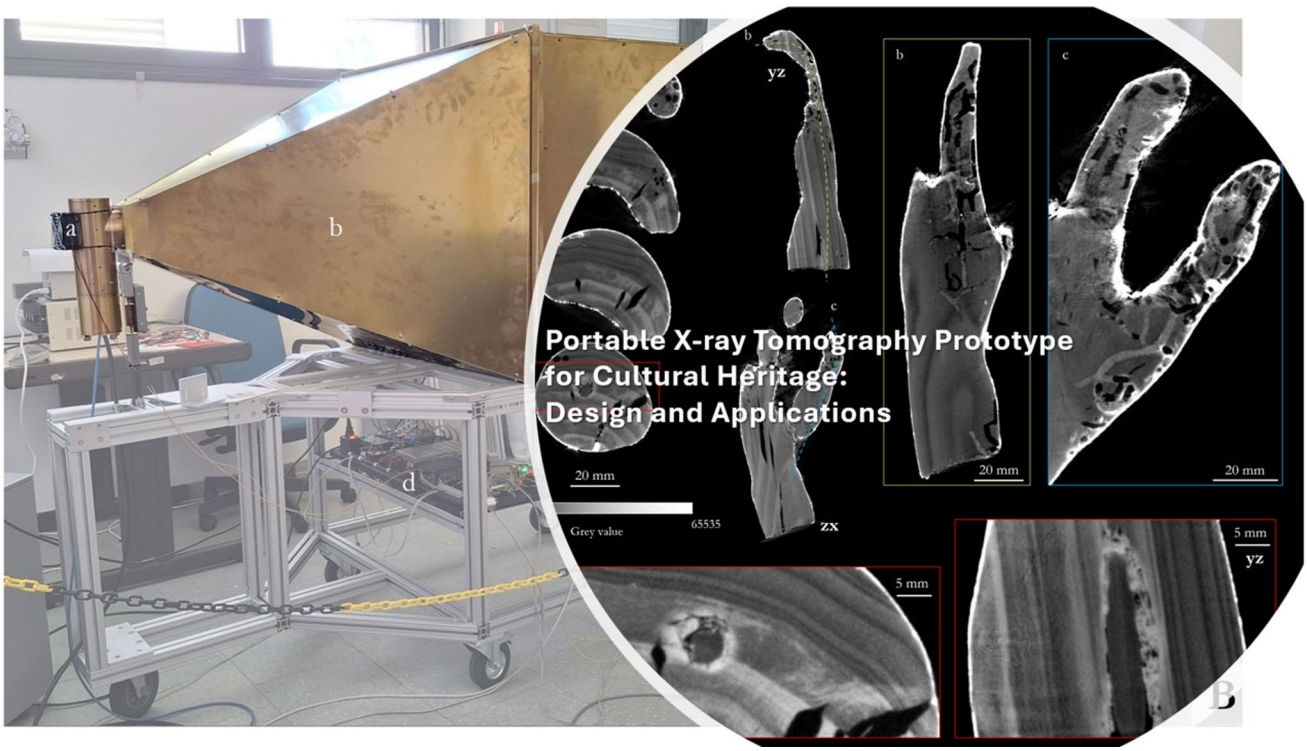

keywords tomography · radiography · portable instrumentation · imaging · Cultural Heritage · PNRR · CHANGES foundation

1 Introduction

X-ray radiography and tomography are widely employed as non-invasive and non-destructive methods in Heritage Science, as evidenced by the numerous projects where these methods played a crucial role (Casali 2006; Albertin 2019; Vigorelli et al. 2022; Lehmann and Mannes 2021). Advanced X-ray radiography and computed tomography (CT) have become indispensable non-destructive tools in the study and conservation of cultural heritage artefacts - ranging from wooden statues and bone artifacts to polychrome sculptures and archaeological finds.

These techniques may reveal internal features such as cracks, previous restorations, internal supports, wood grain patterns, and material stratigraphy - insights inaccessible by visual inspection alone (Re et al. 2014; Bossema et al. 2024; Withers et al. 2021). For example, CT imaging has been used to document internal iron supports and insect damage in medieval wooden sculptures (Kapit 2016), and to perform non-invasive dendrochronology on historical panel paintings, uncovering concealed double panelling (Domínguez-Delmás et al. 2021).

X-ray radiography and computed tomography (CT) were traditionally applied to cultural heritage (CH) studies using medical CT scanners, an approach that remains valid in many cases. However, hospital CT systems are inherently optimised for human anatomy, calibrated to specific density ranges and geometries, and are not easily adaptable to the heterogeneous materials, morphologies and dimensions typically encountered in CH artefacts. This limitation is particularly critical when the tomographic investigation represents the first non-invasive assessment of an object's material structure and conservation state. For this reason, custom-made, scalable instrumentation is essential. Moreover, many heritage artifacts are fragile, unmovable, or located on-site where transportation to standard CT facilities is prohibited or risky. Recent efforts have thus focused on portable, flexible X-ray tomography systems, enabling tailored imaging strategies adapted to object size, shape, and conservation constraints.

The prototype presented in this work addresses these needs through a fully shielded, small-scale, modular CT system, which can be transported and reassembled directly within conservation laboratories, thereby avoiding the risk of moving fragile objects. The need for transportable

systems is already discussed and addressed in other scientific papers, such as (Oliveira et al. 2022; Bettuzzi 2017). Tunable up to 50 kV and 1 mA (maximum), the system is optimised for low- to medium-density samples of limited thickness. Its soft X-ray beam enables high-contrast imaging of delicate organic materials, which would otherwise appear nearly transparent under the higher energy spectra of conventional medical or industrial sources. This combination of transportability, adaptability and low-energy operation makes the instrument particularly suited to the wide morphological and compositional variability inherent to cultural heritage materials.

This work was carried out within the framework of the CHANGES project, through the collaboration between the Department of Physics and Astronomy of the University of Florence, the Cultural Heritage network of the Italian National Institute of Nuclear Physics (INFN-CHNet), and the Department of Physics and Astronomy of the University of Bologna. The instrument was designed and developed by the INFN Florence group, drawing on previous expertise in cultural heritage imaging instrumentation (Mazzinghi et al. 2024) and, in particular, on the design and installation of NICHE, the first Italian neutron imaging station dedicated to cultural heritage applications (Gelli et al. 2023; Grazzi et al. 2023; Grazzi et al. 2025). The project also benefited from the partnership of the Opificio delle Pietre Dure, which acted as end-user, providing consultancy and test samples that were instrumental for the development and optimisation of the system.

2 Instrument design

2.1 Description of the portable X-ray tomograph

The tomographic system described in this work is a compact and portable cone-beam X-ray CT scanner specifically developed for the non-destructive imaging of small low Z artefacts in the field of cultural heritage. Its design prioritises low weight, modularity, and ease of deployment, while ensuring radiation safety even outside designated radioprotection environments. The instrument is fully self-shielded (see Sect. 2.2: Radiation Safety), featuring a protective enclosure made of 1.2 mm thick brass plates mounted on a lightweight aluminium frame, which also supports all ancillary elements. The fact of being self-shielded is one of the differences between the instrument developed by the research group of Prof. Morigi (UniBo), which is transportable as this one but requires an appropriate space to address radiosafety rules (Bettuzzi 2017).

The structure is mounted on wheels to facilitate mobility. Additional shielding is integrated along the beam path to attenuate primary and secondary radiation (see Sect. 2.2: Radiation Safety). A leaded-glass window (2.1 mm Pb equivalent) allows direct visual monitoring of the sample during operation. The system's geometry is defined with the Y-axis aligned with the X-ray beam (positive towards the detector), the Z-axis oriented vertically (positive upwards), and the X-axis perpendicular to the beam (positive left to right when facing the detector). The measurement chamber accommodates objects up to 800 mm in height, although the field of view (FoV) is currently limited to 300 × 300 mm. No automated vertical stage is yet installed; the Z-position must be manually adjusted. A schematic of the instrument is shown in Fig. 1.

The X-ray source is a compact low-power unit (Oxford X-Ray Unit Jupiter 5000 Series, 50 kV, 1.0 mA (Oxford, 2025), enclosed within a stainless-steel housing with dielectric oil for thermal regulation and an external 6 mm leaded bronze shield (CC497K - CuSn5Pb20-C) to enhance radiation protection. It features a molybdenum target, operates at 10–50 kV, and delivers a 23° cone beam with a nominal focal spot of 150 µm. The system includes dual fans providing active air cooling.

The flat-panel detector (Teledyne DALSA Xyneos 3030HS (Dalsa 2024) is based on a CsI scintillator using radiation-hard CMOS Active Pixel design, 16-bit depth. It offers an active area of 295 × 295 mm² with 1952 × 1952 pixels and a nominal pixel size of 151.8 µm.

Motion control is achieved through a compact linear stage supporting a high-precision rotational stage (Physik Instrumente PI-037), driven by a closed-loop DC motor with an integrated encoder. The stage enables rotational accuracy at the microradian scale, with negligible backlash and high repeatability, essential for reliable projection sampling.

The internal chamber of the instrument can accommodate objects up to 700 mm in height and more than 300 mm in diameter. However, considering the field of view (FoV) and the beam size at the sample *(see Sect. 3)*, the maximum sample dimensions for the present configuration are approximately 200 mm in diameter and 500 mm in height when the object cannot be inverted. In this case, two vertical scans are acquired without altering the position of the rotation axis. If the sample can be inverted, objects up to 600 mm in height can be measured.

A summary of key technical specifications is provided in Table 1.

2.2 Radiation safety

The entire system is clad with 1.2 mm thick brass panels, while the X-ray tube is enclosed within an external 6 mm leaded bronze shield (CuSn5 Zn5 Pb5 UNI 7013-72). The access door to the sample area (300 × 800 mm²) is also

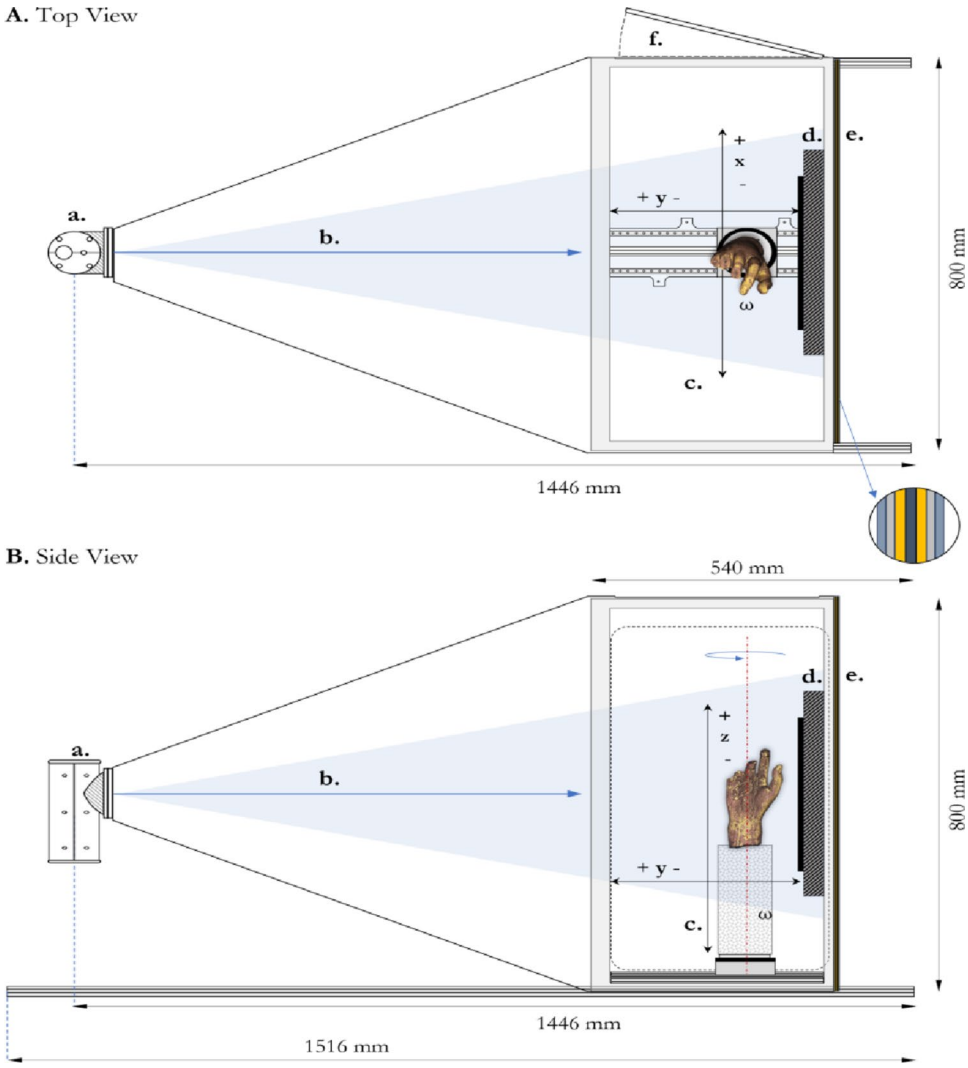

Fig. 1 Schematic overview of the instrument: top view (**A**) and side view (**B**). (**a**) X-ray source; (**b**) beam; (**c**) sample environment with a holder equipped with a translator along the beam axis (y-axis) and a rotator; the height can be adjusted by adding modular spacers according to sample requirements; (**d**) flat-panel detector; (**e**) multilayer beam-stop wall: PVC (1.0 mm); aluminium (1.0 mm); brass (1.2 mm); lead (1.2 mm); brass (1.2 mm); aluminium (1 mm); PVC (1 mm); (**f**) lateral access door to the sample area (30 × 80 cm²)

constructed from 1.2 mm thick brass. On the opposite wall, a leaded glass window is installed to allow visual inspection of the sample area during positioning and measurement. The window (20 cm × 10 cm) provides a lead equivalence of 2.1 mm and ensures full shielding for X-ray energies up to 150 keV.

Behind the detector, a multilayer beam-stop wall is installed with the following configuration, from the outside in (the shielding was intentionally oversized in case of higher-voltage and higher-current tubes): PVC (1 mm), absorbing low-energy characteristic X-rays from aluminium (e.g. 1.47 keV); aluminium (1 mm), attenuating X-rays generated in the underlying brass layer (Zn and Cu, < 10 keV); brass (1.2 mm), absorbing lead characteristic radiation (10–14 keV); lead (1.2 mm), acting as the main absorber and attenuating primary X-rays up to 50 keV; brass (1.2 mm), further reducing lead X-ray emissions directed inward; aluminium (1 mm), attenuating residual radiation from the preceding brass layer; and PVC (1 mm), providing the final inner layer to minimise low-energy background on the detector (Fig. 2).

The system is equipped with multiple interlocks that immediately disable X-ray generation upon door opening, emergency stop activation, or intrusion into a monitored safety area (1.5 × 1.5 m) around the instrument. Radiation dose measurements under maximum output (50 kV, 1 mA) indicate dose rates below background at the boundary of the safety area (0.2 µSv/h), and a maximum of ~ 12 µSv/h at the shielding surface. This confirms its safe use in environments without dedicated radioprotection infrastructure, including public spaces.

Table 1 Technical specifications of the portable CT scanner

Component	Specification
X-ray source	Oxford X-Ray Unit type XTF5011, 50 kV, 1.0 mA, Mo target, 150 µm spot, 23° cone, 75 µm Be window
Source shielding	Internal lead-lined casing + external 6 mm Pb-bronze + Choterm® (thermal conductor, electrical insulator)
Source Cooling system	Dielectric oil + dual fan cooling (150 cfm), operating temperature < 55 °C
Detector	Flat panel Teledyne DALSA Xyneos 3030HS, CsI scintillator, 1952 × 1952 px, 16-bit depth
Nominal Pixel size	151.8 µm
SDD	1301.6 mm
FoV	295 × 295 mm²
Motion stages	Y-axis Linear: ball-bearing rail; Rotational: PI-037 minimum increment 3.5 µrad
Max object size	H: 600 mm Ø: 250 mm
Frame structure	Aluminium (20 × 20 mm² profile), modular and lightweight
External shielding	1.2 mm brass + Beam stop wall: graded multi-layer (PVC–Al–Brass–Pb–Brass–Al–PVC)
External dimension	H: 800 mm; W: 800 mm; L: 1446 mm
Overall weight	150 kg

3 Instrument characterization

To provide sharp images, cone-beam tomographic reconstruction algorithms require accurate geometric characterization of the instrument. In this section, it is briefly described how this was achieved.

The two fundamental input parameters in this regard are the so-called "Source to Detector Distance" (SDD) and "Object to Detector Distance" (ODD). Determining these by relying on the design of the instrument can be difficult as one should not only precisely control distances, dimensions and alignments of the mechanical components, but also know the distance between the CCD plane and the outer shell of the X-ray detector, and the distance between the geometric origin of the X-ray conical beam and the beryllium window of the tube. As such, it turns out to be more convenient to determine SDD and ODD by performing ex-post calibration measurements once the instrument is fully assembled. Such a calibration can be repeated to account for potential small variations in the geometry of the instrument, e.g., after it has been transported to a new location.

Calibration is performed as follows: a square sample object, shown in Fig. 3, with lateral dimension ℓ (12 ± 0.005 cm) was prepared and placed on the rotary stage. The sample consists in a 0.1 mm-thick brass plate with an array of 11×11, 0.1 mm precisely machined round holes with 10 mm grid spacing.

For a given position of the linear stage, we acquire a frame and measure the length of the projected image on the detector (which is readily obtained as the pixel size is

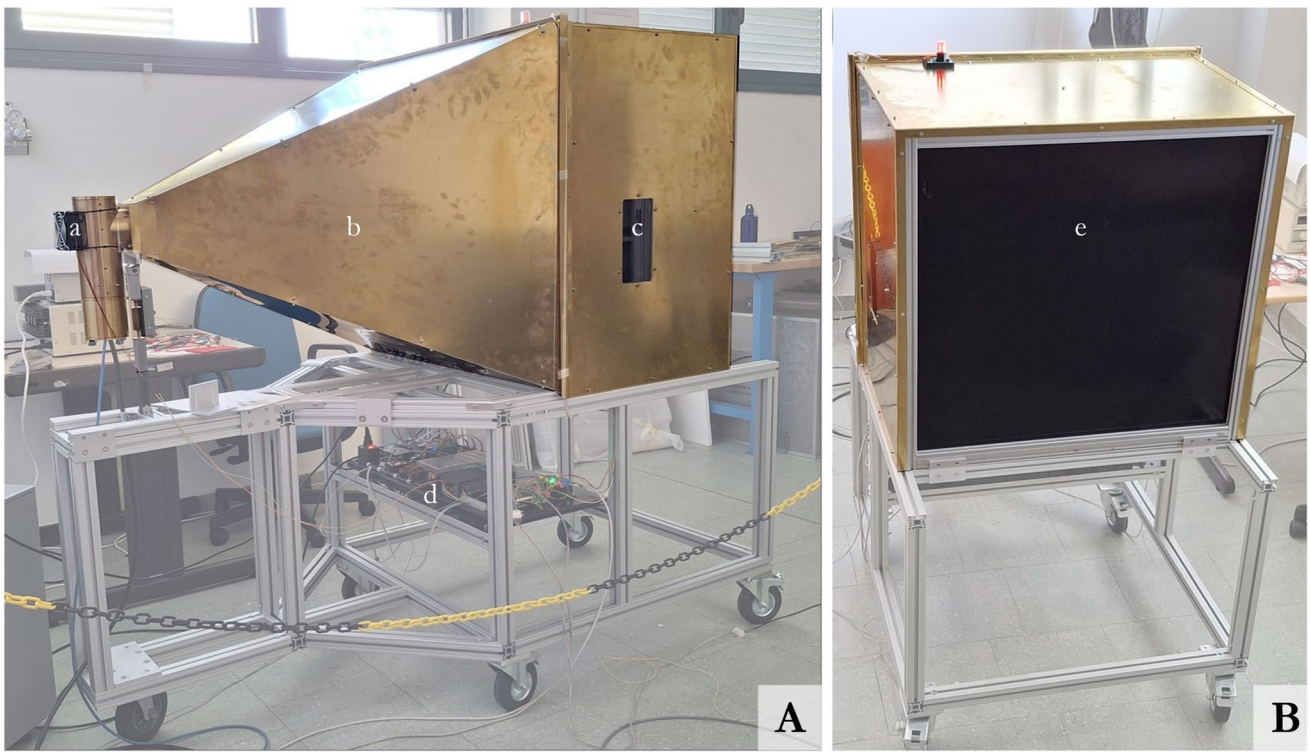

Fig. 2 Tomograph shielding. (**a**) Source shielding: cylindrical enclosure made of 6.0 mm thick leaded bronze; (**b**) 1.2 mm thick brass sheets covering the entire system and following the conical shape of the beam; (**c**) leaded glass window; (**d**) dedicated electronics shelf positioned away from the beam and easily accessible; (**e**) multilayer beam-stop wall

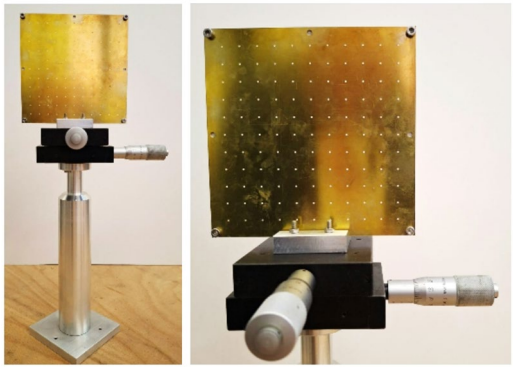

Fig. 3 Sample object employed for test measurements of SDD

Table 2 Technical parameters measured of the portable CT scanner

SDD	1301 ± 0.5 mm
ODD	327.2 ± 0.2 mm ("Home" position of the linear stage)
Tilt angle	0.032 ± 0.002 deg
Beam centre	(971.5 ± 0.2 px, 966.3 ± 0.2 px)

known). With this single measurement, one can only infer the ratio between SDD and ODD.

A second measurement is then performed in which the linear stage is moved towards the detector by a known fixed amount Δ. If we denote by L_1 and L_2 the length of the first and second projections, then:

$$\mathrm{SDD} = \frac{\Delta}{\not{\ell}} \frac{L_1 L_2}{L_1 - L_2}$$

Having two projections with different ODDs also allows us to determine the centre of the beam, i.e., the pixel coordinates of the point where the beam hits the detector orthogonally. Provided the linear stage itself is orthogonal to the detector, the centre of the beam corresponds to the fixed point in the homothety describing the transformation between the two images. Finally, we need to determine the position of the rotation axis and its tilt with respect to the detector. This is trivially done by comparing two projections, at 0 deg and 180 deg respectively. The results of the measurements of all the above parameters are summarised in (Table 2).

4 Acquisition software

The project also focused on the development of a custom-made open-source software controlling data acquisition and all parameters needed for a tomography. The tomograph is controlled through custom-made open-source software written in C++. Although currently running on Linux on x86-64 hardware, the program is designed to be portable by using technologies available across different operating systems and architectures, namely the Qt 6 toolkit for the user interface and the OpenCV computer vision library for image processing. A modular design ensures the possibility of extending the support to different hardware, making the acquisition program suitable to be used with other computerized tomography instruments.

The program manages hardware by means of a multi-threaded architecture and leverages the native signal/slot mechanism of Qt, allowing for easy communication among different threads, thus avoiding blocks in the main thread handling the user interface. The motors driving the linear and the rotary stage are controlled by Arduino Mega 2560 Rev3 boards paired with custom-designed shields. Each Arduino board communicates with the PC through a single RS-485 multi-drop serial bus in a half-duplex configuration. The RS-485 bus is handled by a dedicated secondary thread in the acquisition program. Requests to the hardware are queued in the Qt event-loop of the dedicated QThread and dispatched synchronously, thus ensuring the atomicity of each Request/Reply pair in the half-duplex communication protocol.

The Xineos-3030HS X-ray detector communicates with the PC through a Gigabit Ethernet data interface, using a driver that implements the GigE Vision standard. Frames are grabbed by running dedicated jobs in a thread pool.

The graphical user interface (shown in Fig. 4) provides access to all relevant hardware parameters, including:

- Full Well Capacity and Exposure Time for the X-ray detector;
- X-ray tube output (voltage and current);
- sample positioning through control of the linear and rotary stages.

The acquisition of a full tomography is handled automatically by the program, after the projection angles are either selected on the user interface or input through custom scripts for additional flexibility.

Projection frames get automatically pre-processed in two steps. The first step consists of standard flat-field correction using dark-current and open-beam frames. In the second step, the image is corrected by replacing defective pixels with the median average of neighbouring pixels. The defective-pixel map used for image correction is provided by a careful analysis of the linearity in the response of each individual pixel of the X-ray detector, obtained by taking frames with varying exposure times.

Projection frames are then exported in TIFF file format, either as individual files or as a single multi-page TIFF file, ready to be processed by the tomographic reconstruction software of choice.

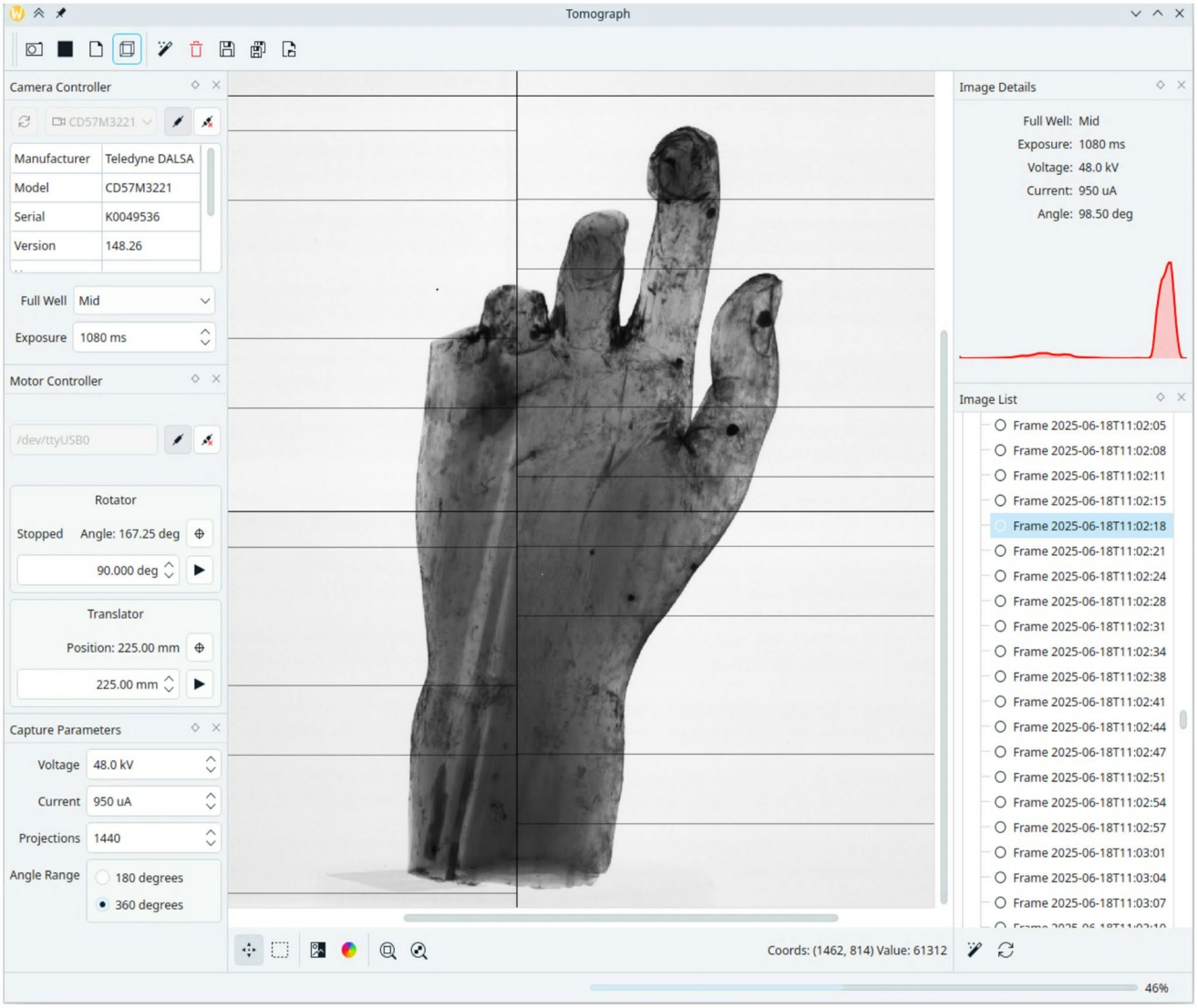

Fig. 4 Main screen of the acquisition software developed for the prototype tomograph: on the left, the control panel allows the measurement parameters to be configured; on the right, the interface displays the progress of the ongoing scan; at the top, the histogram of the image provides real-time feedback on the quality of the acquired data

Alongside these, a text file is produced, containing the relevant geometric parameters necessary to run the cone-beam reconstruction algorithm.

5 Experimental characterization on test samples

A series of proof-of-concept experiments were conducted on objects with diverse dimensions, morphologies and material compositions to evaluate the prototype's performance in relation to some of most typical Cultural Heritage materials (i.e. wood and bones) and define optimal acquisition parameters. The number of projections for each scan was estimated using the Nyquist–Shannon sampling theorem and adjusted according to the specific question on each sample. Similarly, the tube current and voltage were tuned to optimise the contrast of the material under investigation. For wooden specimens with thicknesses between 100 mm and 500 mm, for instance, operating conditions of 40 kV and 0.9 mA were found to enhance contrast between wood fibres while ensuring adequate penetration of the sample.

All acquired datasets underwent pre-processing (such as cropping when needed, filters, and initial simple image editing) normalisation and reconstruction. Owing to the excellent signal-to-noise ratio of the images, no additional denoising filters (such as *Despeckle* or *Remove Outliers*) were required. Defective pixels were removed directly

using the defective-pixel map as described in Sect. 4. As the acquisition software allows export of raw datasets, normalisation can be performed using any image-processing platform (e.g. ImageJ). Alternatively, the option to export already normalised images enables immediate access to the radiographs, even for operators without expertise in imaging data treatment. Tomographic reconstruction was performed using *MuhRec* (Kaestner 2011), an open-source tool that supports cone-beam reconstruction, rotation-axis correction and dynamic-range optimisation prior to full-volume reconstruction. Visualisation, reslicing and all 2D image operations were carried out in ImageJ/Fiji (Rueden and Eliceiri 2019; Goldstein et al. 2017), while 3D volume rendering and segmentation routines were performed in the open-source software 3D Slicer (Fedorov et al. 2012). The resulting tomographic datasets consist of 16-bit images in which attenuation is represented along a grey-scale range of 0–65,535. In principle, a value of 0 corresponds to transparent media and is associated with the background; when reconstruction is performed with dynamic-range clipping, the background can effectively be fixed at zero.

Three representative examples were selected from the numerous samples analysed. They include two wooden specimens - a recent boxwood cylindrical sample and a fragment from a historical statue (the right hand of a late 13th -century Italian painted wooden statue) - and an undated bone sample from archaeological excavation consisting of a rib from a male individual. The wooden samples were kindly made available by the Department of Conservation of Wooden Artifacts of the Opificio delle Pietre Dure in Florence and are typically used as models for study, research and training within the activities of the master's degree in Conservation. The bone sample was kindly made available by the radiocarbon dating research group of the LABEC laboratory (Chiari et al. 2021).

The acquisition parameters for the samples are summarized in Table 3.

5.1 Spatial resolution and contrast resolution estimation

Once the radiographic stack has been normalised or the reconstruction stage has been completed, it is mandatory to evaluate the image quality and, as with any set of experimental data, to estimate its uncertainty. The quality of an image is mainly determined by two factors: spatial resolution and contrast resolution. The effective spatial resolution (SR) is evaluated by analysing the sharpness of edges within the image. To this end, a line profile (plot profile) is extracted across a transition region—for example, from a dense, X-ray-opaque object to the surrounding air—on an axial slice. Ideally, such a profile would exhibit a sharp edge, with an abrupt transition from high to low grey values. In practice, however, this transition is smoothed due to blurring effects, and the resulting profile shows a gradual change in intensity. This gradient reflects the system's point spread function and thus the effective SR. Since Cultural Heritage artefacts often have highly complex geometries, establishing the SR solely through instrumental parameters is not typically sufficient. Once an estimate has been obtained, it may still be necessary to verify on the tomographic slice the operational value that can reasonably be assigned to describe the smallest resolvable detail. In Fig. 5a, for example, a high-contrast region of an axial slice—such as the edge of the Boxwood sample against the background—is shown. As can clearly be observed, the edge blurring extends over more than a single pixel. The edge profile allows the uncertainty in domain discrimination to be quantified. To measure sharpness, the edge profile is fitted using a sigmoidal Boltzmann function. The minimum distance over which the transition occurs—typically measured between the inflection point (centre of the fit) and the tails—is taken as an estimate of the blurring. In the present case, despite a pixel size reduction due to geometric magnification (from 151.8 µm to an apparent 130 µm, corresponding to a magnification factor of ~1.15), the measured edge spread indicates a blurring of approximately 160 µm. This value defines the actual SR of the reconstructed tomographic slice. Once the SR of our images has been measured, dimensional analysis can be carried out. As an example, Fig. 5b shows a detail of a circular cross-section hole in the Boxwood test sample. The diameter of the hole was estimated by analysing the intensity profile along a linear section (see Fig. 5) and assuming the actual distance as the full width at half maximum (FWHM) of the intensity. This evaluation incorporates the previously assessed edge sharpness, ensuring that the measured dimension accounts for the effective spatial resolution of the dataset (2.02 mm ± 0.16 mm). Some features close to this threshold—such as wood grain patterns, made visible by subtle local density variations—remain discernible. This demonstrates the system's ability to capture fine structural details even down to the nominal resolution level.

Table 3 Acquisition parameters. SDD: Sample-Detector distance; SOD: Source-Object Distance; ODD: object detector Distance. Edge resolution is meant as clarity and sharpness of edges in the images

Sample	SDD (mm)	SOD (mm)	ODD (mm)	Magnification factor	*N*° projections	Voxel size (mm)	Edge resolution (mm)
Boxwood	1301.6	1109.5	192.1	1.17	720	0.130	0.161
Statue hand	1301.6	1155.5	146.1	1.13	1440	0.135	0.180
Rib	1301.6	985.5	320.2	1.32	720	0.115	0.130

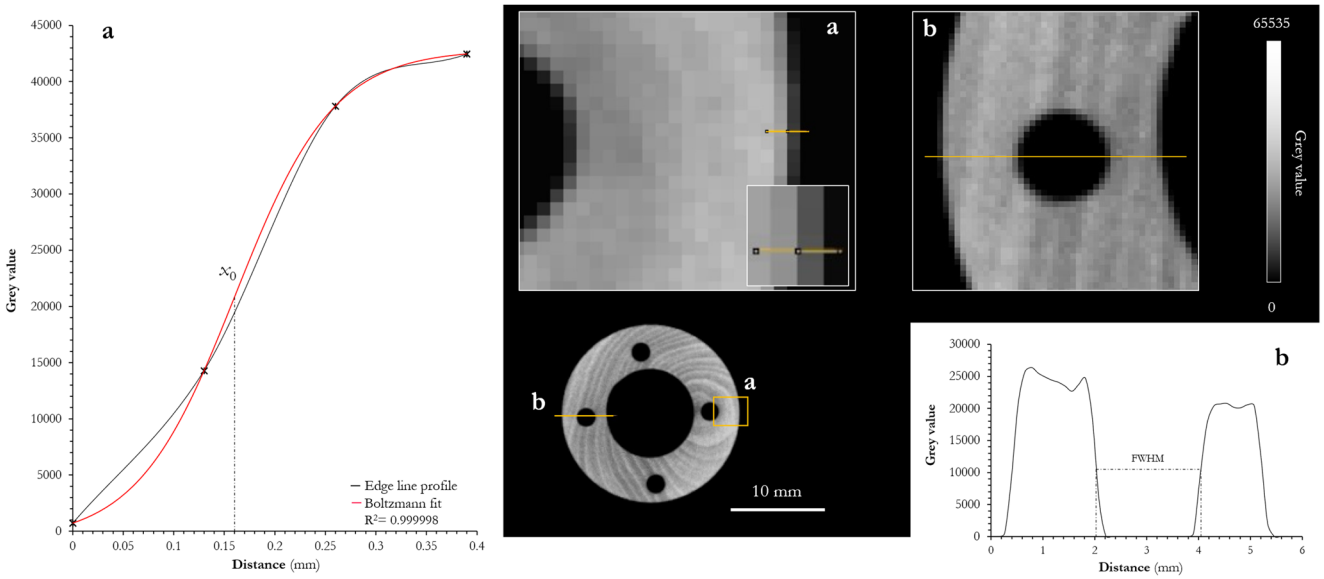

Fig. 5 Evaluation of the effective spatial resolution and dimensional accuracy of the Boxwood test sample. **(a)** High-contrast region of an axial (xy-plane) slice showing the edge between the sample and the background. The inset highlights the transition region used for the edge profile analysis. The red curve represents the fitted sigmoidal Boltzmann function used to estimate the edge spread. **(b)** Detail of a circular cross-section hole within the sample. The intensity profile along the yellow line was used to measure the hole diameter using the FWHM, incorporating the previously assessed edge sharpness to account for the effective spatial resolution of the dataset

In standard radiographs and X-ray CT images, wood anatomical features such as earlywood and latewood are readily distinguishable: earlywood exhibits lower attenuation and appears darker due to its lower density and thin-walled cell structure, whereas latewood appears lighter as a result of its higher lignin content and thicker cell walls. These differences in density and cellular morphology enable the clear visualisation of growth rings. Similarly, heartwood often shows higher attenuation than sapwood due to its greater density and extractive content, allowing for the non-destructive discrimination between these tissues (Ellis 1971; Koubaa et al. 2002; Wang et al. 2019). To test the capability of our system in distinguishing morphological and microstructural details, we evaluated the tonal contrast achieved by our imaging setup.

Contrast resolution (CR) (also indicated as tonal sensitivity) refers to the ability to distinguish materials with different attenuation coefficients. In digital images, this parameter depends directly on noise levels and the intrinsic properties of the materials. When analysing homogeneous regions, the standard deviation of the grey values measured within a selected area can be considered as the uncertainty in the tonal evaluation of a material. An alternative approach to assess CR is the Signal-to-Noise Ratio (SNR), which provides a combined measure of both noise and contrast. In principle, image noise can be estimated in any uniform region of the image. To illustrate this, an axial slice showing a close-up of the wood microstructure in the Boxwood sample is presented in Fig. 6. Mean grey values were extracted from regions of interest (ROIs) corresponding to low-attenuating and high-attenuating wood phases, as well as from the background of the slice. The three selected zones were assumed to be homogeneous: (I) high-attenuation area ("latewood"), (II) low-attenuation area ("earlywood"), and (III) background.

The signal-to-noise ratio (SNR) was calculated according to $SNR = |\mu s - \mu b|/\sigma b$, where μs and μb represent the mean intensities of the selected phase and background, and σb is the background standard deviation. This method provides a quantitative evaluation of the tomographic contrast. The analysis yielded SNR values of 32.6 for the low-attenuating regions (sapwood) and 43.9 for the high-attenuating regions (heartwood) relative to the background. Furthermore, the SNR directly calculated between sapwood and heartwood is 8.6, confirming the reliability of the measurement in discriminating the wood microstructure of earlywood and latewood in terms of grey levels.

5.2 Results

Among the test samples used for the tomographic study, two wooden specimens were included: a recent boxwood cylinder and a historical artefact, the hand of a painted wooden statue (unknown species). For the boxwood cylinder, Fig. 7 shows several views of the reslice of the sample, displayed both in a conventional greyscale and using a thermal colour scale to enhance the internal microstructure.

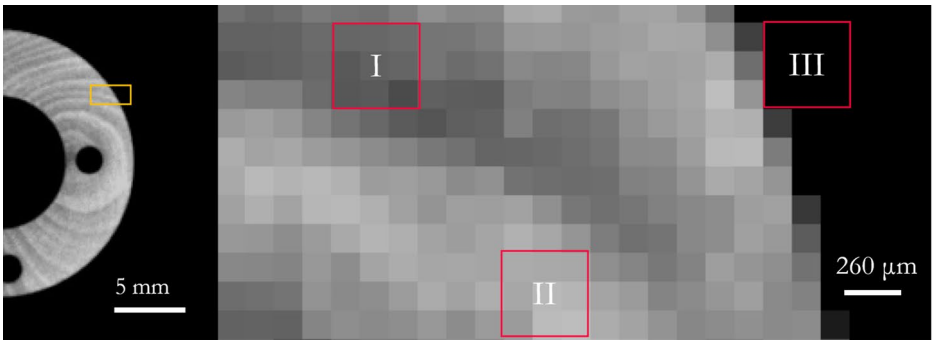

	ΔS	σ_{bkg}	SNR
I - III	30498.0	936.7	32.6
II - III	41077.0	936.7	43.9
II -I	10579.0	1228.3	8.6

Fig. 6 SNR approach for the evaluation of contrast resolution. Axial slice of the boxwood sample showing a close-up of the wood microstructure. On the left, an overview of the sample is displayed; the orange box marks the enlarged area shown on the right. Three homogeneous regions of interest (ROIs) are highlighted: (I) high-attenuation area ("latewood"), (II) low-attenuation area ("earlywood"), and (III) image background. These regions were used to estimate tonal sensitivity and to calculate SNR as reported in the table on the right

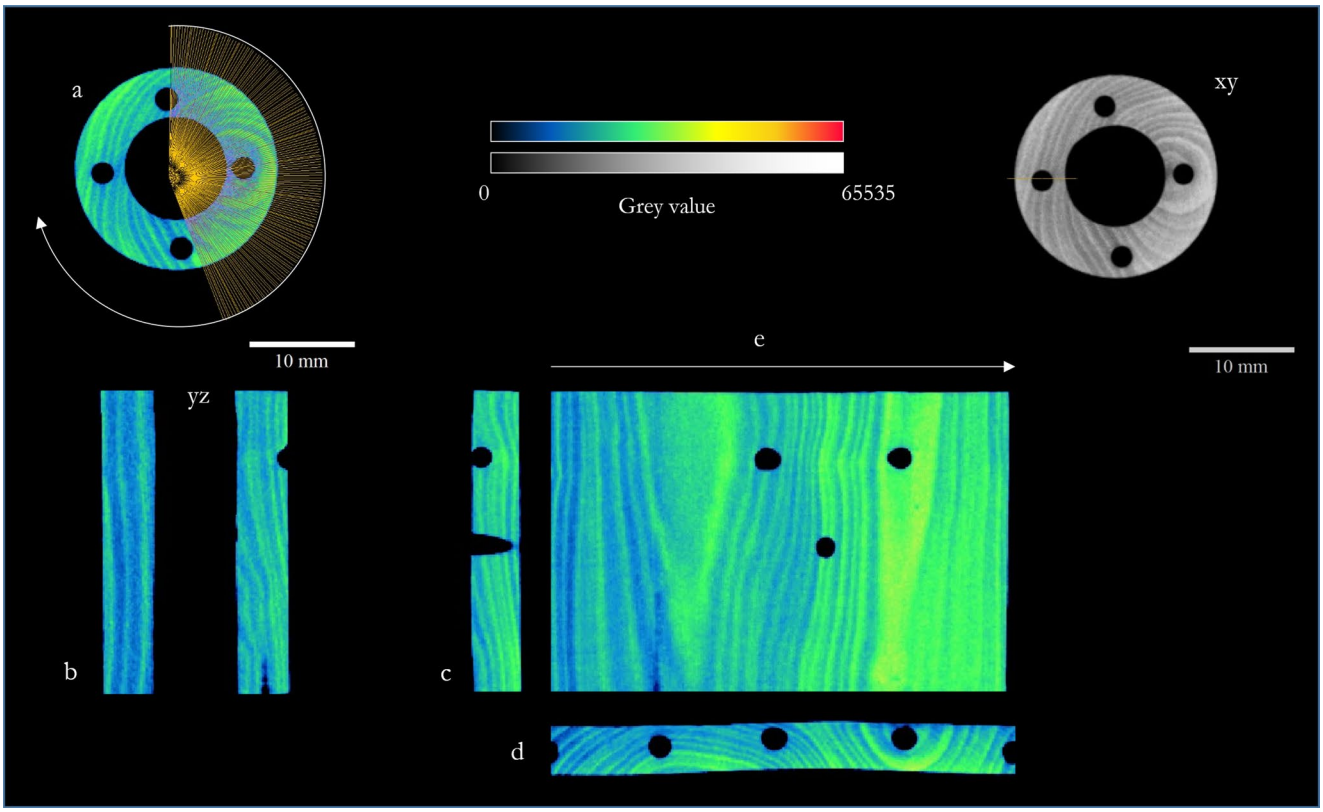

Fig. 7 Radial reslice visualisation of the Boxwood sample.(**a**) Schematic of the radial reslice procedure using the ImageJ radial reslice tool: the line ROI (yellow) is rotated around its centre to generate orthogonal slices.(**b**) Conventional sagittal section (yz) of the sample in thermal scale, highlighting the internal microstructure.(**c**) Individual orthogonal slice obtained through the radial reslice tool.(**d**) Resliced stack viewed from above, displaying the circumferential sections.(**e**) Unfolded circumferential views spread onto a single plane. The thermal colour scale enhances subtle variations in grey value to reveal the wood's internal structure. The image in (**e**), though geometrically distorted compared to the axial slices, provides an effective overall view of the sample's morphology

Considering the cylindrical geometry of the sample, to visualise the internal microstructure more effectively on a single plane, instead of using sagittal or orthogonal sections, the images were digitally rectified using, for example, the ImageJ radial reslice tool. This plugin generates orthogonal reconstructions of an image stack by rotating a line ROI around either one of its ends or its centre (Fig. 7a). This approach is particularly effective for systems with cylindrical symmetry (e.g. the bodies of wind instruments) but it can also be employed to visualise concave shell-like structures. The procedure described here is similar to the one we used in (Sans-Planell et al. 2023). First, a line ROI is drawn, which defines the radius of rotation. Each of the orthogonal slices generated therefore corresponds to a different angular

view (Fig.7c). This stack can then be resliced either from above (Fig. 7d) or from the side (Fig. 7e), depending on the requirements. The resliced stack (**e**) contains the circumferential views unfolded and displayed on a single plane. Although the resulting image is distorted and of lower quality compared to the axial sections, it provides an effective overall view of the sample and allows for a precise morphological study of the internal walls.

X-ray tomography of a wooden statue fragment, painted with a Pb/Hg-based layer, revealed complex internal features within the palm section. The axial slice in Fig. 8 highlights the wood microstructure, where the alternating bands of earlywood and latewood are clearly visible as concentric layers with contrasting grey levels. The tonal contrast between these anatomical phases reflects the density difference: earlywood, with its thin-walled cells and lower density, appears darker and less attenuating, whereas the denser, lignin-rich latewood produces lighter, more attenuating bands. The horizontal and vertical line profiles (H and V) plotted across the section capture these variations, displaying periodic oscillations in grey values that correspond to the alternation of growth rings, thereby confirming the preserved microstructural organisation of the timber. In the axial section, three sharp, diamond-shaped cavities (checks) can be also observed.

The histogram on the right provides a visual interpretation of the tonal distribution within the section. The highlighted regions of grey levels correspond to distinct material densities: the lowest range relates to the voids and cracks; the intermediate peaks represent earlywood and latewood; higher attenuation levels indicate the heartwood zone, while the brightest region corresponds to the Pb-based paint residues containing also Fe and Hg traces and its preparation layer (attested by the presence of Ca), as indicated by XRF spectroscopy carried out by means of the instrument developed by INFN-CHNet (Taccetti et al. 2019). It is worth noting that CT is not suitable for discriminating different pigments in terms of composition, but other analytical methods - such as XRF - are needed for the correct identification of the material composition. The latter not only produces

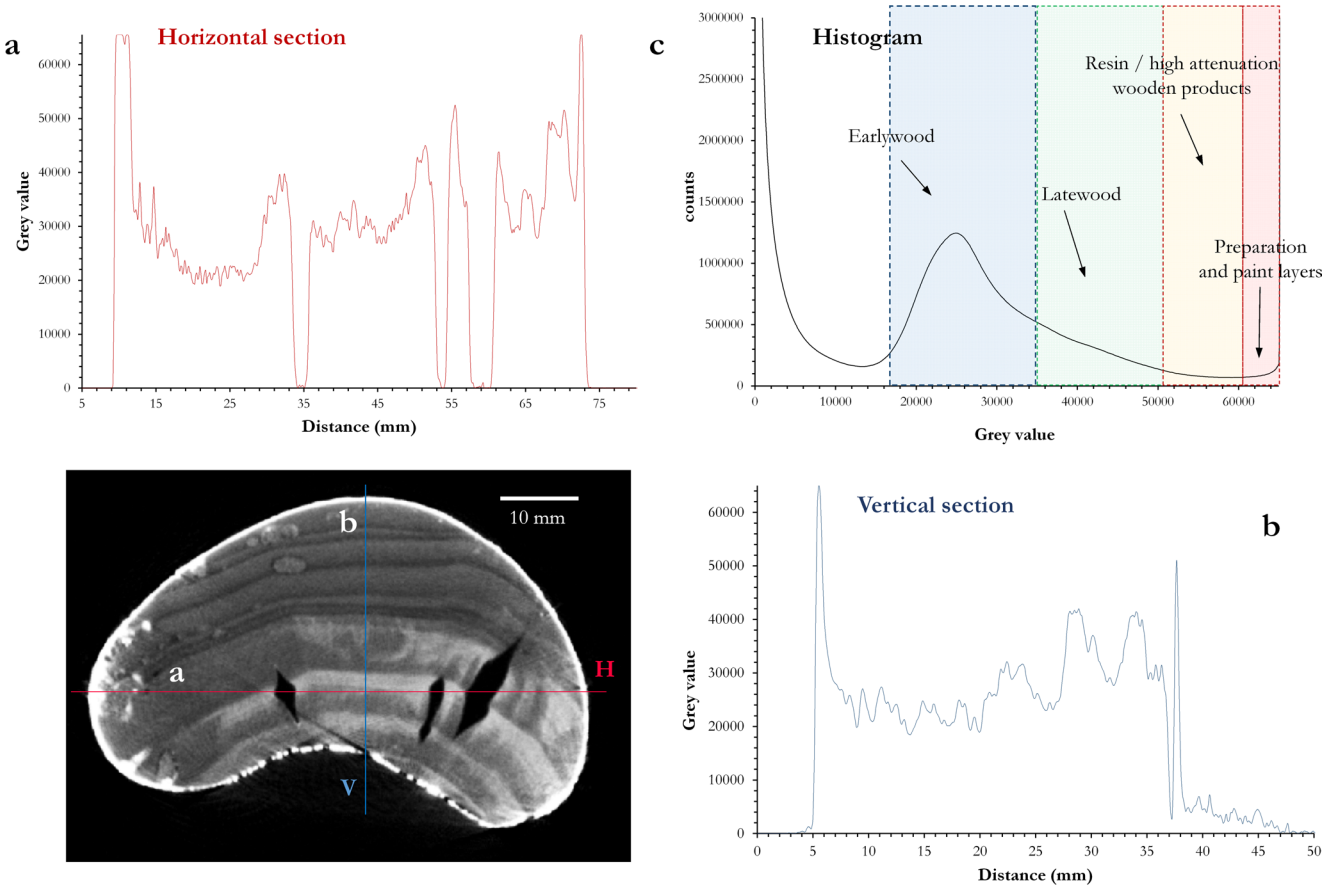

Fig. 8 Axial tomographic slice of the palm from the 13th -century wooden statue fragment, still bearing traces of a Pb/Hg-based painting layer. Alternating earlywood and latewood bands are visible as concentric layers with distinct grey levels, as shown by the horizontal (H) and vertical (V) line profiles and their respective plots (**a**) and (**b**). The three checks, caused by differential shrinkage during ageing are evident, appearing as black diamond shaped cavities. The histogram (**c**) highlights tonal ranges corresponding to earlywood, latewood, and the highly attenuating preparation and paint layers, illustrating the interpretative process linking grey-level distribution to material density

highly attenuating borders in the tomographic slice but also generates minor beam-hardening artefacts visible around the edges. Together, the line profiles and histogram illustrate the effectiveness of the tomographic contrast in resolving the anatomical features, internal degradation, and compositional heterogeneity of the artefact.

In Fig. 9a selection of tomographic slices of the wooden hand is shown, revealing both structural and microstructural features of the artefact. The axial slices (xy) on the left display successive cross-sections of the hand, where the alternating earlywood and latewood bands are clearly distinguishable as concentric rings with different grey levels, reflecting the preserved anatomical organisation of the wood. In these sections, three pronounced longitudinal checks are visible, extending from the wrist area towards the base of the fingers. These fissures, appearing as sharp, diamond-shaped cavities, are thus the result of differential shrinkage during seasoning and long-term ageing. While only partially perceptible on the external surface, they are

Fig. 9 X-ray tomography of the 13th -century statue's hand. Left: axial slices (xy) showing the alternating earlywood and latewood bands and, in the red box, the wrist area containing a wooden dowel likely used for the original joint with the forearm. Bottom: magnified axial and longitudinal views of the dowel (red boxes). Centre: sagittal (yz) and normal (zx) sections; lines b and c indicate the paths used for dynamic reslicing in Fiji/ImageJ to visualise the complex geometry of the fingers, shown in the green and blue frames. The tomograms reveal a dense network of insect galleries, some appearing as empty voids and others partially filled with incoherent material, probably residual frass or compacted sawdust

Fig. 10 X-ray tomography of the human rib. Left: axial (xy) sections showing the thin cortical shell and the internal trabecular (spongy) bone with an alveolar-like architecture. The main inner cortical wall measures approximately 330 µm, while secondary walls are below 200 µm. Right: sagittal (yz) slices highlighting the rib's curvature and the continuity of the cortical layer enclosing the trabecular core. The dataset demonstrates the system's ability to resolve both dense cortical and delicate spongy bone structures in archaeological samples

clearly revealed in the tomographic sections, highlighting significant internal degradation.

The red-highlighted region at the wrist shows a wooden dowel of a different species, likely part of the original jointing system connecting the hand to the forearm. Its distinct attenuation pattern relative to the surrounding heartwood makes it easily identifiable. The magnified axial and longitudinal views (bottom red boxes) emphasise both the circular cross-section of the dowel and its insertion depth into the wood matrix.

The sagittal (yz) and normal (zx) sections provide complementary insight into the object's internal configuration. Because of the complex geometry of the hand, standard orthogonal cuts alone were insufficient to display entire regions of interest on a single plane. To address this, *dynamic reslicing* was applied using Fiji/ImageJ, which enables the generation of sections orthogonal to a curved or segmented line of interest and can combine features lying on different planes.

The cutting paths are indicated by lines (**b**) and (**c**) in the central view, with the resulting reslices shown in the green and blue frames. This method, despite a minor loss of resolution and dimensional accuracy, allowed the continuous visualisation of the fingers and their internal features.

Across all sections, the wood microstructure is well preserved, with clear differentiation between earlywood and latewood as well as heartwood regions. A dense network of insect galleries is distributed throughout the volume. Some tunnels appear as empty voids, while others are partially filled with incoherent, low-density material—most likely residual frass or compacted sawdust trapped after excavation by xylophagous insects. Together, all information extracted through the tomographic analysis about checks, dowel and insect activity provide crucial information on the structural integrity, construction techniques and long-term degradation processes affecting the artefact.

In Fig. 10, X-ray tomography of the human rib is presented, acquired to evaluate the system's performance on bone matrices. The sample was scanned at a magnification of 1.3×, achieving a voxel size of 115 µm and an edge spread of 130 µm. The left panel displays a series of axial (xy) sections, where the rib's anatomical features are clearly resolved. The thin cortical shell is sharply delineated, enclosing an internal trabecular (spongy) structure with a finely preserved alveolar-like architecture. The main inner cortical wall shows a thickness of approximately 330 µm, while secondary internal walls measure below 200 µm, demonstrating the ability of the system to resolve both dense and delicate structures within the same dataset.

The right panel shows sagittal (yz) slices, highlighting the curvature of the rib and the continuity of the cortical layer surrounding the trabecular core. The trabecular bone network is rendered with high definition, allowing the visualisation of the internal alveolar pattern and the interconnected pores typical of spongy bone. Together, the axial and sagittal sections confirm the system's capability to capture microstructural details in archaeological bone samples, preserving both cortical and trabecular features essential for structural and histological assessment.

6 Conclusions and perspectives

In this work it is presented a portable X-ray tomography prototype specifically designed for Heritage Science applications on light attenuating materials and developed within the PNRR CHANGES PE 5 project. The tomograph met all its objectives in developing a simple, robust, reliable, transportable, low power absorption, radiation safe system for radiographies/tomographies of Cultural Heritage artefacts. The hardware and software of the instrument were developed, tested, assembled and are now in their final configuration.

The whole system is intrinsically transportable, its transportability being effectively guaranteed by light weight, sturdy mechanical structure, and the reliability of its control electronics, which have been derived from those developed for MACHINA, the transportable accelerator (Taccetti et al. 2023).

Measurements have shown that the tomograph is safe, as radiation protection is concerned. The authorisation for use even in presence of the public has already been obtained, which is of the utmost importance for using the tomograph at museums, conservation centres and sites where the public can be present. The tomograph will be installed at the Opificio delle Pietre Dure in Firenze, to become part of the instrumentation normally used in the diagnostic activity, by the fall of 2025.

The development of a new instrument is under study, designed to accommodate heavier objects while retaining the detector, drivers, motors, and control electronics currently in use. This ensures full compatibility with the existing control software, reducing costs and maintaining operational continuity.

In parallel, a higher spatial resolution version of the system is under consideration, particularly for applications in palaeontology. A detector with 50-micron pixel size -fully compatible with the current software- has already been identified and can be integrated with only minor adjustments. Additionally, a microfocus X-ray tube that closely matches the requirements of this high-resolution setup has been selected and can be readily installed on the upgraded platform.

The control software will continue to evolve, with updates and refinements based on feedback from the users at the OPD, where the tomograph will be deployed. This user-driven development process will add a significant value over commercial systems, whose software is typically fixed and less adaptable to the specific needs that emerge from daily use in Cultural Heritage diagnostics.

The same control electronics and software developed for the portable X-ray tomograph will also be adopted for the neutron radiography/tomography imaging station at the CHNet unit, installed at the TRIGA reactor in Pavia. This will ensure a unified, flexible, and user-friendly interface across different imaging modalities (X-rays and neutrons), will streamline operator training, and will optimize maintenance and future developments.

Acknowledgements The authors A.M. and L.G. gratefully acknowledge the support of CHANGES (Cultural Heritage Active Innovation for a Next-Gen Sustainable Society) Foundation to the University of Florence (Physics and Astronomy Department), Project PE 0000005 CHANGES—CUP B53C22003780006, NRP Mission 4 Component 2 Investment 1.3, Funded by the European Union—NextGenerationEU". The authors also want to thank all the personnel of the UniFi administrative unit, in particular Dr. Arianna Xekalos, Dr. Emanuela Pasquini and Dr. Teresa Zefiro, whose apport was crucial to end with all the procedures to get the materials.OPD and Bologna research group acknowledge the CHANGES foundation for supporting this project.Dr. Rodrigo Torres Saavedra is kindly acknowledged for starting the communication software with the detector. The authors wish to thank Dr. Rodolfo Panerai for his insightful discussions and invaluable technical support with the hardware and software.Acknowledgement is due to Dr. Francesco Grazzi (CNR-IFAC) for his valuable advice and for providing several wood specimens that served as test samples.Dr. Sara Bassi (OPD), Dr. Mariaelena Fedi and Dr. Lucia Liccioli (INFN-Florence) are warmly acknowledged for sharing the samples employed in this work. The authors are also deeply indebted to INFN-CHNet. Special thanks go to the Bologna Unit, and an even deeper thanks to the Firenze Unit and its personnel, without whom none of this would have been possible.The authors further wish to thank the mechanical workshop of the Department of Physics and Astronomy, University of Florence (Mattia Leporatti, Matteo Puccianti, Alberto Catelani, and Nicola Pasqualetti) for their help and patience in developing the detector holding structure and constructing and improving the shielding and Lorenzo Sodi of the INFN Florence Unit for designing and fabricating the mechanical structure and shielding.

Author contributions A.M. and F.C. equally contributed to this work.L.G. and F.T. conceived the original idea. A.M., L.G., L.C., M. Massi, M. Manetti, F.T. conceived and planned the project. M. Manetti designed the model of the instrument and realized most of the mechanical components of the instrument. M. Massi has designed and implemented the control electronics of the instrument. L.G. and F.T. supervised the project.A.M. and F.C. carried out the measurements. A.M. and F.C. contributed to the interpretation of the results. M.B. and MP.M were involved in planning and supervising the work, particularly regarding the detection system.A.C., M.G., S.P. were involved during the design of the instrument, specifying the needs in quality of end users of the instrument.L.G. prepared the initial draft of the manuscript. F.C. and A.M. revised the manuscript to the final version.All authors discussed the results and contributed to the final manuscript.

Funding Open access funding provided by Università degli Studi di Firenze within the CRUI-CARE Agreement.

Data availability No datasets were generated or analysed during the current study.

Declarations

Competing interests The authors declare no competing interests.

References

Albertin F, Bettuzzi M, Brancaccio R, Morigi MP, Casali F (2019) X-Ray Computed Tomography In Situ: An Opportunity for Museums and Restoration Laboratories. Heritage 2:2028–2038

Bettuzzi M, Morigi MP, Brancaccio R, Peccenini E, Casali F (2017) A mobile computed tomography system for on-site cultural heritage analysis. In Proceedings of the IEEE International Conference on Environment and Electrical Engineering and 2017 IEEE Industrial and Commercial Power Systems Europe (EEEIC / I&CPS Europe), 6–9 June 2017, 2017; pp. 1–6

Bossema FG, Palenstijn WJ, Heginbotham A, Corona M, van Leeuwen T, van Liere R, Dorscheid J, O'Flynn D, Dyer J, Hermens E (2024) Enabling 3D CT-scanning of cultural heritage objects using only in-house 2D X-ray equipment in museums. Nat Commun 15:3939. https://doi.org/10.1038/s41467-024-48102-w

Casali F (2006) X-ray and Neutron Digital Radiography and Computed Tomography for Cultural Heritage. In: Bradley D, Creagh D (eds) Physical Techniques in the Study of Art, Archaeology and Cultural Heritage. Elsevier, Amsterdam

Chiari M, Barone S, Bombini A, Calzolai G, Carraresi L, Castelli L, Czelusniak C, Fedi M, Gelli N, Giambi F et al (2021) LABEC, the INFN ion beam laboratory of nuclear techniques for environment and cultural heritage. Eur Phys J Plus. https://doi.org/10.1140/epjp/s13360-021-01411-1

Dalsa Teledyne Available online: https://www.teledynedalsa.com/en/products/imaging/industrial-x-ray/shad-o-box-hs/ (accessed on 09-02-2024)

Domínguez-Delmás M, Bossema FG, Dorscheid J, Coban SB, Hall-Aquitania M, Batenburg KJ, Hermens E (2021) X-ray computed tomography for non-invasive dendrochronology reveals a concealed double panelling on a painting from rubens' studio. PLoS One 16:e0255792. https://doi.org/10.1371/journal.pone.0255792

Ellis JC (1971) Use of X-rays in measuring ring widths from increment borings. N Z J For Sci 1:223–230

Fedorov A, Beichel R, Kalpathy-Cramer J, Finet J, Fillion-Robin J-C, Pujol S, Bauer C, Jennings D, Fennessy F, Sonka M et al (2012) 3D slicer as an image computing platform for the Quantitative Imaging Network. Magn Reson Imaging 30:1323–1341. https://doi.org/10.1016/j.mri.2012.05.001

Gelli N, Giuntini L, Cantini F, Sans-Planell O, Magalini M, Manetti M, Sodi L, Massi M, Castelli L, Czelusniak C et al (2023) The new INFN-CHNet neutron imaging facility. Nuclear Instruments and Methods in Physics Research Section A: Accelerators, Spectrometers, Detectors and Associated Equipment 168189. https://doi.org/10.1016/j.nima.2023.168189

Goldstein JI, Newbury DE, Michael JR, Ritchie NWM, Scott JHJ, Joy DC (2017) ImageJ and Fiji. Scanning Electron Microscopy and X-Ray Microanalysis. Springer, New York, pp 187–193

Grazzi F, Cantini F, Gelli N (2025) The New NICHE Imaging Station at the TRIGA-Reactor in Pavia. Available online: https://www.isnr.de/images/NR-Newsletter/nr17.pdf (Accessed on 30/05/2024)

Grazzi F, Cantini F, Sans-Planell O, Magalini M, Vigorelli L, Marcucci G, Clemenza M, Morigi M, Re A, Alloni D (2023) A work-horse neutron imaging station at the Laboratorio Energia Nucleare Applicata (LENA) in Pavia (Italy): instrumental components and applications in the frame of the CHNet-NICHE INFN experiment. Journal of Physics: Conference Series 2605:012006. https://doi.org/10.1088/1742-6596/2605/1/012006

Kaestner AP (2011) Muhrec—a new tomography reconstructor. Nucl Instrum Methods Phys Res Sect A 651:156–160. https://doi.org/10.1016/j.nima.2011.01.129

Kapit á ny K, Somogyi A, Barsi A (2016) Inspection of a medieval wood sculpture using computer tomography. In Proceedings of the The International Archives of the Photogrammetry, Remote Sensing and Spatial Information Sciences, Prague, Czech Republic, ; pp. 287–291

Koubaa A, Zhang SYT, Makni S (2002) Defining the transition from earlywood to latewood in black Spruce based on intra-ring wood density profiles from X-ray densitometry. Ann Sci 59:511–518

Lehmann E, Mannes D (2021) Chapter 5 - Neutron and X-ray tomography in cultural heritage studies. In: Adriaens M, Dowsett M (eds) Spectroscopy, Diffraction and Tomography in Art and Heritage Science. Elsevier, pp 133–159

Mazzinghi A, Castelli L, Ruberto C, Barone S, García-Avello Bofías F, Bombini A, Czelusniak C, Gelli N, Giambi F, Manetti M et al (2024) X-ray and neutron imaging for cultural heritage: the INFN-CHNet experience. Eur Phys J Plus 635. https://doi.org/10.1140/epjp/s13360-024-05429-z

Oliveira R, de Paula A, Gonçalves F, Bueno R, Calgam T, Azeredo S, Araújo O, Machado A, Anjos M, Lopes R et al (2022) Development and characterization of a portable CT system for wooden sculptures analysis. Radiat Phys Chem 110409. https://doi.org/10.1016/j.radphyschem.2022.110409

Oxford, Jupiter (5000) (2025) Available online: https://xray.oxinst.com/x-ray-tube-products/x-ray-tube-assembly-radiation-shielded/jupiter-5000-series (Accessed on 08/09/2025)

Re A, Albertin F, Avataneo C, Brancaccio R, Corsi J, Cotto G, De Blasi S, Dughera G, Durisi E, Ferrarese W (2014) X-ray tomography of large wooden artworks: the case study of "Doppio corpo" by Pietro Piffetti. Herit Sci 2:19. https://doi.org/10.1186/s40494-014-0019-9

Rueden CT, Eliceiri KW (2019) ImageJ for the next generation of scientific image data. Microsc Microanal 25:142–143. https://doi.org/10.1017/S1431927619001442

Sans-Planell O, Cantini F, Costa M, Durisi E, Grazzi F, Mafucci E, Monti V, Bedogni R, Li Y (2023) Improved methodologies to study the performance of the ANET Compact Neutron Collimator. Nuclear Instruments and Methods in Physics Research Section A: Accelerators, Spectrometers, Detectors and Associated Equipment 1052:168260. https://doi.org/10.1016/j.nima.2023.168260

Taccetti F, Castelli L, Czelusniak C, Gelli N, Mazzinghi A, Palla L, Ruberto C, Censori C, Lo Giudice A, Re A et al (2019) A multipurpose X-ray fluorescence scanner developed for in situ analysis. Rend Fis Acc Lincei 30:307–322. https://doi.org/10.1007/s12210-018-0756-x

Taccetti F, Castelli L, Chiari M, Czelusniak C, Falciano S, Fedi M, Giambi F, Mandò PA, Manetti M, Massi M et al (2023) MACHINA, the movable accelerator for cultural heritage in-situ non-destructive analysis: project overview. Rend Fis Acc Lincei 34:427–445. https://doi.org/10.1007/s12210-022-01120-6

Vigorelli L, Re A, Buscaglia P, Manfredda N, Nervo M, Cavaleri T, Del Vesco P, Borla M, Grassini S, Guidorzi L et al (2022) Comparison of two ancient Egyptian Middle Kingdom statuettes from

the Museo Egizio of Torino through computed tomographic measurements. J Archaeol Sci Rep 103518. https://doi.org/10.1016/j.jasrep.2022.103518

Wang Q, Liu Xe, Yang S, Jiang M, Cao J (2019) Non-destructive detection of density and moisture content of heartwood and sapwood based on X-ray computed tomography (X-CT) technology. Eur J Wood Wood Prod 77:1053–1062. https://doi.org/10.1007/s00107-019-01459-y

Withers PJ, Bouman C, Carmignato S, Cnudde V, Grimaldi D, Hagen CK, Maire E, Manley M, Du Plessis A, Stock SR (2021) X-ray computed tomography. Nat Rev Methods Primers 1:18. https://doi.org/10.1038/s43586-021-00015-4